Design and Performance of an Aeroacoustic Wind Tunnel Facility at the University of Bristol

Yannick D. Mayer[a], Hasan Kamliya Jawahar[a], Máté Szőke[a], Syamir Alihan Showkat Ali[a], Mahdi Azarpeyvand[a,*]

[a]*Faculty of Engineering, University of Bristol, United Kingdom*

Abstract

This paper provides an overview of the design and performance of the new aeroacoustic wind tunnel facility at the University of Bristol. The purpose of the facility is to enable near- and far-field acoustic and aerodynamic studies on a variety of different aerodynamic components and to examine diverse noise control techniques. The facility comprises a large acoustic chamber, anechoic down to 160 Hz, and a temperature controlled closed-circuit wind tunnel with an open test section. The wind tunnel features two interchangeable rectangular nozzles with a partially shared contraction. Both nozzles are shown to possess a high flow quality with high flow uniformity and low turbulence intensity of 0.09% and 0.12% for the smaller and larger nozzle, respectively. The maximum attainable flow speeds are 40 m/s for the larger nozzle and 120 m/s for the smaller nozzle corresponding to Reynolds numbers of 2.7 million and 8.1 million per meter, respectively. In this paper, we will present various aerodynamic and acoustic results to characterize the performance of the facility. The background noise levels are found to be sufficiently low and the far-field noise measurements from a flat plate, a round cylinder and a NACA 0012 airfoil compare favorably to existing experimental observations.

Keywords: Aeroacoustics, Wind Tunnel Design, Trailing Edge Noise, Nozzle Design

*Corresponding author: m.azarpeyvand@bristol.ac.uk, Queen's Building, University Walk, BS8 1TR, Bristol, United Kingdom.

A preliminary version of this paper was presented at the 2018 AIAA/CEAS Aeroacoustics Conference in Atlanta, United States [1].

1. Introduction

The sound radiated from bodies immersed in a flow field is of major concern for the aerospace, automotive, civil engineering and wind energy sector, amongst many others. More stringent noise emission regulations all over the globe have made sound reductions a key design driver in many engineering applications nowadays [2]. Several numerical, analytical and experimental studies have been carried out in the past decades to improve our understanding of aerodynamic noise sources.

Notwithstanding the improvements in the computational methods utilized for aeroacoustic predictions in recent years, it is still not feasible to predict the noise emitted by complex flows in various applications. This calls for the inevitable need for well-equipped aeroacoustic facilities to conduct experimental studies. This can help both the fundamental understanding of noise generation mechanisms from different aerodynamic components, such as wings, blades, landing gear systems, cavities, *etc.* [3], and more importantly the development of novel and tailored passive or active flow/noise control methods, such as serrations [4–7], porous treatments [8, 9], morphing surfaces [10, 11], flow suction and blowing [12, 13], *etc.* In the past, the majority of the aeroacoustic wind tunnels have been operated by automotive and aerospace corporations, as well as national institutions, such as NASA, JAXA, NLR and DLR [14–18]. However, over the course of the past 20 years, several universities have been commissioning aeroacoustic wind tunnels of varying sizes and capabilities [19–28]. More recently, Kevlar-walled anechoic wind tunnel test sections have been designed and implemented [8, 28, 29], which improves the aerodynamic performance of the wind tunnel, while keeping the flow acous-

tically accessible.

Open-jet wind tunnels are widely used to conduct aeroacoustic measurements. In order to enable high-quality research, an open-jet aeroacoustic facility has to fulfill several requirements. It has to deliver a flow with low turbulence intensity and high flow uniformity across the nozzle exit plane, a very low background noise level, as well as near anechoic conditions for high accuracy noise measurements [20]. The background noise of open-jet type anechoic wind tunnels consists of the jet noise, fan noise and noise generated by the flow passing through the individual components of the wind tunnel as well, as vibration caused structure-borne noise. With careful design, the fan noise and the self-noise of the wind tunnel components can be significantly attenuated, leaving the noise of the free jet as a limiting factor for background noise [19, 20].

This paper discusses the design and performance of the aeroacoustic wind tunnel facility at the University of Bristol. The purpose of this facility is to perform near- and far-field acoustic characterizations on a variety of different bodies and aerodynamic components. The facility will be used for absolute noise measurements or relative noise tests to evaluate the effects of noise reduction techniques. A detailed overview of the facility and its individual components is presented in Section 2. Subsequently, Section 3 will outline the acoustic and aerodynamic characteristics of the wind tunnel and far-field noise benchmark cases of a flat plate, a cylinder, two NACA 0012 airfoils and a 30P30N high-lift device. These test cases are chosen to demonstrate the capabilities and performance of the facility for a wide range of fundamental and engineering applications.

2. Wind Tunnel Design Overview

The Aeroacoustic facility at the University of Bristol is a closed-circuit, open-jet anechoic wind tunnel, designed for aerodynamic and aeroacoustic studies. Figure 1 displays an isometric view of the wind tunnel without any surrounding building structures and without the anechoic chamber. A top view of the facility, including the surrounding structures and anechoic chamber, is provided in Fig. 2 and a cut-section side view through the forward-leg of the wind tunnel can be seen in Fig. 3. The entire facility was designed to fit within an available space of 16.6 m in length, 6.8 m in width and 4.6 m in height in the existing wind tunnel laboratory of the University of Bristol. A directly driven centrifugal fan (part A in Figs. 1 - 3) expels air into the forward-leg of the wind tunnel which houses two silencers (parts B & C) and a section with acoustic wall treatment (part D). Consequently, the flow is turned and passed through the settling chamber (part E) before it is accelerated through the contraction nozzle (part F). The free jet is caught by a collector (part H) which channels the flow through two silencers (parts I & J) and a heat exchanger (part K) in the return-leg back to the centrifugal fan. All corners are equipped with turning vanes with a chord of 192 mm manufactured out of 1.5 mm rolled mild steel with chamfers at the leading and trailing edge. Additionally, the ductwork is designed to be fully airtight in order to avoid the emergence of any noise due to flow leakage.

A closed-loop feedback control allows both the temperature and velocity to be set and maintained, permitting continuous operation of the wind tunnel facility under a wide range of ambient conditions ensuring repeatability of any measurements conducted.

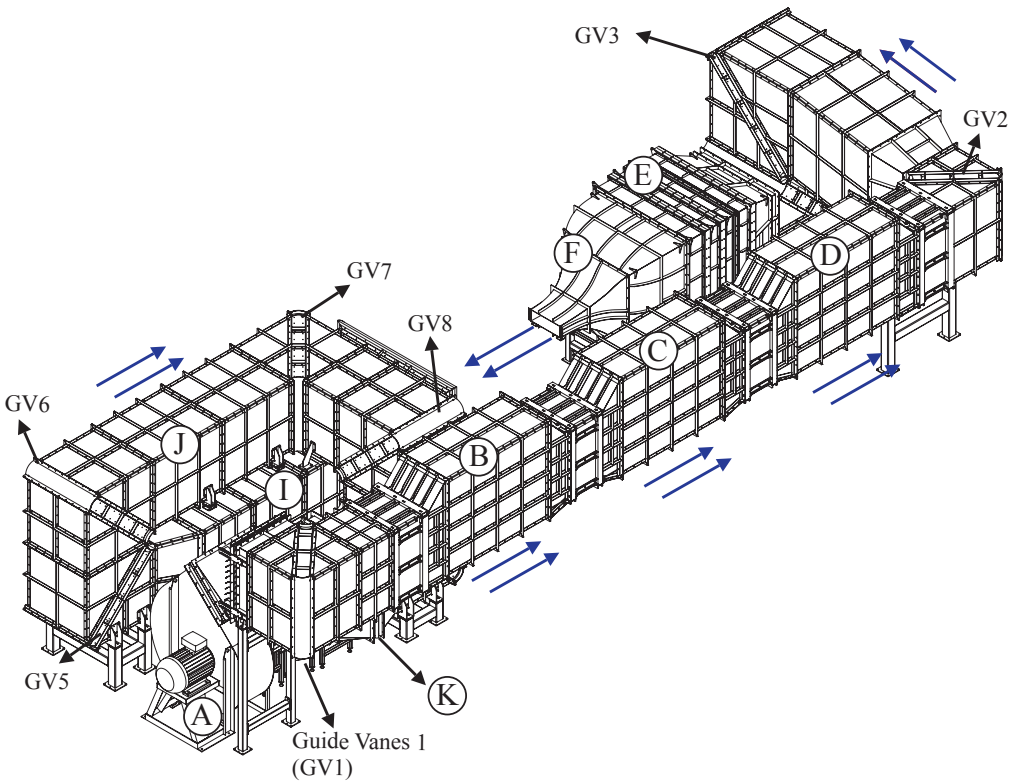

Figure 1: Isolated isometric view of the aeroacoustic wind tunnel and its components. Blue arrows are indicative of the local flow direction. (A) Centrifugal fan, (B) Silencer 1, (C) Silencer 2, (D) Lined duct, (E) Settling chamber, (F) Nozzle, (I) Silencer 3, (J) Silencer 4, (K) Heat exchanger.

The design currently features two nozzles of the following sizes, 600 mm × 200 mm (Nozzle 1) and 500 mm × 775 mm (Nozzle 2), which will be discussed in Section 2.4. The following sections will describe the design and features of the different wind tunnel components in greater detail.

2.1. Centrifugal Fan and Heat Exchanger

The centrifugal fan (part A) drives air through the wind tunnel and was sized according to the chosen design operating conditions ($\dot{Q}$, ΔP) for each nozzle, an overview of

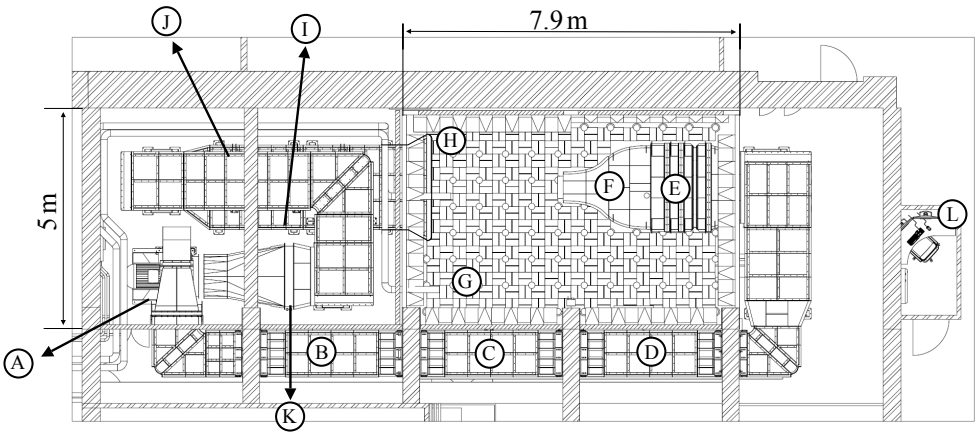

Figure 2: Top view of the aeroacoustic facility including external control room. (A) Centrifugal fan, (B) Silencer 1, (C) Silencer 2, (D) Lined duct, (E) Settling chamber, (F) Nozzle, (G) Anechoic chamber, (H) Collector, (I) Silencer 3, (J) Silencer 4, (K) Heat exchanger, (L) Control room.

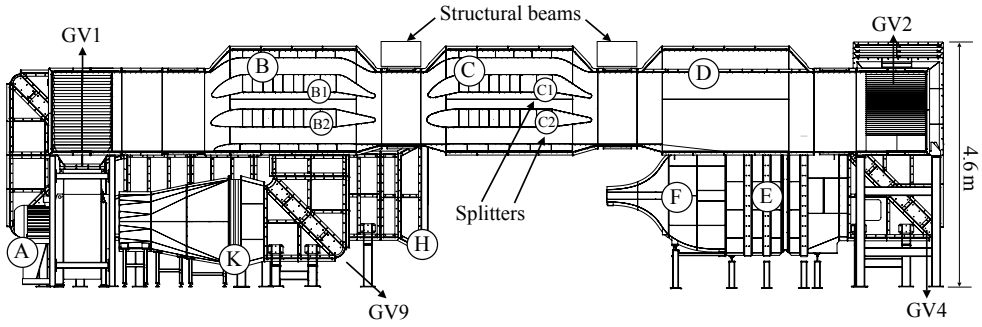

Figure 3: Section side view through the forward-leg of the aeroacoustic wind tunnel. (A) Centrifugal fan, (B) Silencer 1, (C) Silencer 2, (D) Lined duct, (E) Settling chamber, (F) Nozzle, (H) Collector, (K) Heat exchanger.

which can be seen in Table 1. The larger nozzle (Nozzle 2), requiring a volumetric flow rate of 15.3 m^3/s and static pressure rise in excess of 3000 Pa, drives the fan specifications more than the smaller nozzle (Nozzle 1). As a result of this, the maximum velocity attainable with Nozzle 1 will be in excess of the design velocity of $U_\infty = 60$ m/s at the contraction nozzle exit. The selected centrifugal fan is a direct drive Ferrari FQ1121/N4A fan with a single inlet and outlet which absorbs up to 55 kW power. The fan is placed at a distance of about 6 m from the anechoic chamber inside an acoustically isolated room. In order to dampen out structural vibration being transmitted through the floor into the anechoic chamber anti-vibration mounts are used to isolate the centrifugal fan from the floor. The fan room is separated from the anechoic chamber by means of two thick walls with high transmission loss, the details of which can be found in section 2.3. The fan allows continuous and stable operation from a minimum volumetric flow rate of 1.5 m^3/s up to the respective design conditions for each nozzle. The velocity at the nozzle exit can be set from two control panels, one inside the anechoic chamber and one in the dedicated control room. The control of the centrifugal fan is then achieved through a closed-loop feedback control system utilizing the pressure drop across the contraction nozzle as input. Lastly, the rate at which noise is emitted into the ductwork from the fan inlet and outlet is summarized in Table 2 for both design conditions, as provided by the manufacturer for the specified operating conditions.

The air entering the fan passes through a heat exchanger (part K), as seen in Fig. 3 to control the temperature of the air flow, utilizing chilled water as a coolant. The employed finned tube heat exchanger directs the air flow through an array of fins and copper tubes which allows heat to be removed up to a rate of 50 kW. In a similar fashion

Table 1: Overview of the fan design conditions.

	Contraction exit dimensions	Design velocity at nozzle exit [m/s]	Static pressure rise, ΔP [Pa]	Volumetric flow rate, $\dot{Q}$ [m^3/s]
Nozzle 1	600 mm × 200 mm	60 (120 achievable)	2970	7.2
Nozzle 2	500 mm × 775 mm	40	3104	15.3

Table 2: Octave band centrifugal fan inlet and outlet sound power for both nozzle design conditions, as provided by the manufacturer.

	f [Hz]	63	125	250	500	1000	2000	4000	8000
Nozzle 1,	Inlet [dB]	87	89	90	91	88	86	86	83
60 m/s	Outlet [dB]	90	92	93	94	91	89	89	86
Nozzle 2,	Inlet [dB]	97	99	100	101	98	96	96	93
40 m/s	Outlet [dB]	100	102	103	104	101	99	99	96

to the velocity control, the flow temperature, within a temperature range of 10 °C to 30 °C, can also be set from the control panels, which in turn controls the heat exchanger through a closed-loop feedback control system to achieve the set temperature.

2.2. Silencers

The duct silencers play an important role in the overall performance of any aeroacoustic wind tunnel facility. The silencers must be designed to provide maximum noise reduction, while producing little self-noise, due to the flow interactions with the silencers, and also causing minimum pressure loss across the duct network. This facility has a total of four large air silencers, with two placed in the forward-leg (parts B and C) and the other two in the return-leg (parts I and J), as illustrated in Fig. 1. Each silencer has been optimized to achieve the required acoustic dynamic insertion loss, *i.e.* the achieved noise reduction including the regenerated flow self-noise, and at the same time maintaining a well-behaved flow. The splitters of each silencer have an aerodynamically shaped solid

leading and trailing edge made from 1.5 mm thick galvanized perforated steel sheets. In between the leading and trailing edge, the splitters are manufactured from perforated galvanized steel filled with compressed acoustic grade mineral wool slab. The airway sections of each silencer are equal in size and do not vary along the flow direction until the trailing edge area is reached. The dynamic insertion loss predictions in this section are based on experimental data obtained from the manufacturer for the respective face flow velocity as well as flow direction of each silencer and takes both the acoustic absorption as well as the regenerated self-noise into account.

2.2.1. Forward-leg Silencers

The forward-leg of the wind tunnel duct system, i.e. from the fan outlet, contains two large silencers (parts B and C), as shown in Figs. 1 - 3. Both silencers have a length of 2800 mm, a width of 920 mm and a height of 1710 mm, and consist of two 120 mm thick modules at the top and bottom of the section and two 300 mm thick central splitters, resulting in the three horizontal airways with a constant height of 290 mm. The splitters, as well as the top and bottom modules, are made out of 1.5 mm galvanized perforated steel sheets, with 3 mm diameter holes equispaced at a pitch of 5 mm. The space behind the perforated sheets is filled with acoustic grade mineral wool slabs for noise attenuation. The leading edge of the bottom splitter of the second silencer (part C2) follows the shape of a symmetric airfoil, whilst the remaining three leading edges of the splitters of both silencers (parts B1, B2, C2) are derived for optimum flow conditions, see Fig. 3. Subsequent to the second silencer, the flow passes through a plain weave mesh screen to smoothen the airflow such that the leading-edge noise of subsequent guide vanes (GV2)

Table 3: Predicted octave band dynamic insertion loss in flow direction from fan to anechoic chamber at the design conditions for both nozzles, based on experimental data from the manufacturer.

f [Hz]	63	125	250	500	1000	2000	4000	8000
Nozzle 1 [dB]	33	39	58	61	54	48	41	41
Nozzle 2 [dB]	29	38	54	58	54	46	43	41

is reduced. The top of the next duct section (part D) has also been lined in the same way, i.e. perforated sheets and acoustic grade mineral wool slabs, to provide further noise attenuation, as illustrated in Fig. 3. The predicted total dynamic insertion loss in the flow direction from the fan to the anechoic chamber is given in Table 3 for both nozzle design conditions.

2.2.2. Return-leg Silencers

After the flow has passed through the anechoic chamber, it is caught by a bell-mouth collector (part H) and channeled back into the ductwork toward the fan inlet. The collector is mounted on the acoustic wall and its inlet is placed just inside the anechoic chamber. The collector inlet has internal dimensions of 2.3 m in width and 1.9 m in height and was sized and placed to ensure that the expanding free jet, as well as downward deflected flows, can be captured, and thereby limiting the interference noise between the free jet and the collector. The collector is lined with a thick layer of acoustic foam to minimize flow interaction noise. Consequently, the flow passes through the two silencers in the return-leg (parts I and J), before it reaches the centrifugal fan after the heat exchanger, see Fig. 1. The silencers in the return duct are oriented vertically and the airways between the splitters have a constant width of 300 mm. All leading edges are circularly shaped and the splitters are made in the same way as the forward-leg silencers.

Table 4: Predicted octave band dynamic insertion loss against the flow direction from fan to anechoic chamber at the design conditions for both nozzles, based on experimental data from the manufacturer.

f [Hz]	63	125	250	500	1000	2000	4000	8000
Nozzle 1 [dB]	24	41	51	52	43	36	46	45
Nozzle 2 [dB]	23	42	56	56	50	43	47	45

The leading and trailing edge are solid and the voids between 1.5 mm thick perforated steel sheets are again filled with compressed acoustic grade mineral wool slab. The first silencer (part I) is 3500 mm long, 1800 mm wide and 1350 mm high, and it consists of two 150 mm thick side modules and two 300 mm thick central modules. The flow will then pass through a second splitter silencer (part J) in the return-leg, consisting of two 150 mm thick side modules and one 300 mm wide central splitter. The silencer has a total length of 2900 mm, as well as a width and height of 1200 mm. The predicted total dynamic insertion loss of these two silencers, i.e. from the fan to the anechoic chamber, is given in Table 4 for both nozzle design conditions.

2.3. Anechoic Chamber

The airtight anechoic chamber has external dimensions of 7.9 m in length, 5.0 m in width and 4.6 m in height, including the surrounding acoustic walls, as outlined in Fig. 2. In order to provide personnel access to the chamber an open mesh raised plastic-fiberglass flooring is employed. All walls, as well as the ceiling and the floor, are covered in wedges with base dimensions of 300 mm $\times$ 300 mm to completely absorb any sound reflections. The wedges on the ceiling have a length of 800 mm whereas all other wedges have a length of 340 mm and the internal wedge tip-to-tip dimensions are 6.7 m length, 4.0 m width and 3.3 m height. Additionally, the exposed surfaces of the ductwork (parts

Table 5: Measured and predicted octave band acoustic wall transmission loss.

f [Hz]	63	125	250	500	1000	2000	4000
Predicted TL [dB]	29	34	36	40	45	49	51
Measured TL [dB]	29	42	52	53	54	57	64

E and F) are acoustically lined to ensure that no reflective surfaces exist within the anechoic chamber. The anechoic chamber has been certified using the ISO 26101 free-field qualification procedure and was found to enable anechoic measurements down to 160 Hz according to the ISO 3745 standard testing procedures for both pure tone and broadband testing for characteristic source dimensions of 0.65 m or less. Additionally, it was determined that the anechoic chamber provides background noise levels equivalent to a noise rating of NR8.

The chamber's four-inch-thick acoustic walls have a high transmission loss (TL) to avoid any external noise sources, such as the fan noise or noise from other wind tunnels, to contaminate the measurements conducted inside the chamber. Table 5 provides the measured and predicted transmission loss of the acoustic wall and it is evident that the measured transmission loss exceeds the predicted transmission loss. The predicted transmission loss was provided by the manufacturer while the measured transmission loss testing was conducted in accordance with ISO 140-4 testing procedures. All wind tunnel components inside the anechoic chamber (settling chamber, nozzle, collector) are made such that they can be removed and the chamber can then be utilized as a fully anechoic chamber.

When the anechoic chamber is used in its usual aeroacoustic configuration, far-field

noise measurements can be conducted using an array of microphones mounted on an arc. The arc itself is mounted to the ceiling via a unistrut mounting channel and aligned with the center point of the nozzle and the free stream direction. The microphone array consists of 1/4" GRAS 40PL type microphones, with a high dynamic range of 32 - 150 dB(A) and a flat frequency sensitivity response between 10 Hz and 20 kHz. The diaphragms of the microphones are mounted along an arc with a radius of 1.75 m. The microphone arc spans over 125° in total, with the microphones placed at regular intervals of 2.5° allowing up to 51 microphones to be used simultaneously. This allows far-field noise measurements to be conducted at polar angles ranging from 25° to 150°. The focal point of the arc can be positioned along the axial nozzle direction, in order to accommodate measurements of bodies with varying sizes. Care was taken such that the expanding jet from the wind tunnel nozzle does not impinge onto the microphones. A photo of the anechoic chamber with an experimental test setup in place including the far-field microphone arc is displayed in Fig. 4.

2.4. Contraction Nozzles and Settling Chamber

The contraction nozzle and the settling chamber are key to obtain a well-behaved flow at the nozzle exit, with low turbulence intensity and low flow angularity whilst achieving a spatially uniform steady stream of air. The wind tunnel currently has two nozzles with the exit cross-sectional areas of 600 mm × 200 mm and 500 mm × 775 mm. The larger nozzle maintains low blockage factors when used for high-lift devices, airfoils at high angles of attack, as well as for bluff bodies. The smaller nozzle can achieve higher velocities and can be used for airfoils at low angles of attack, flat plates and boundary layer

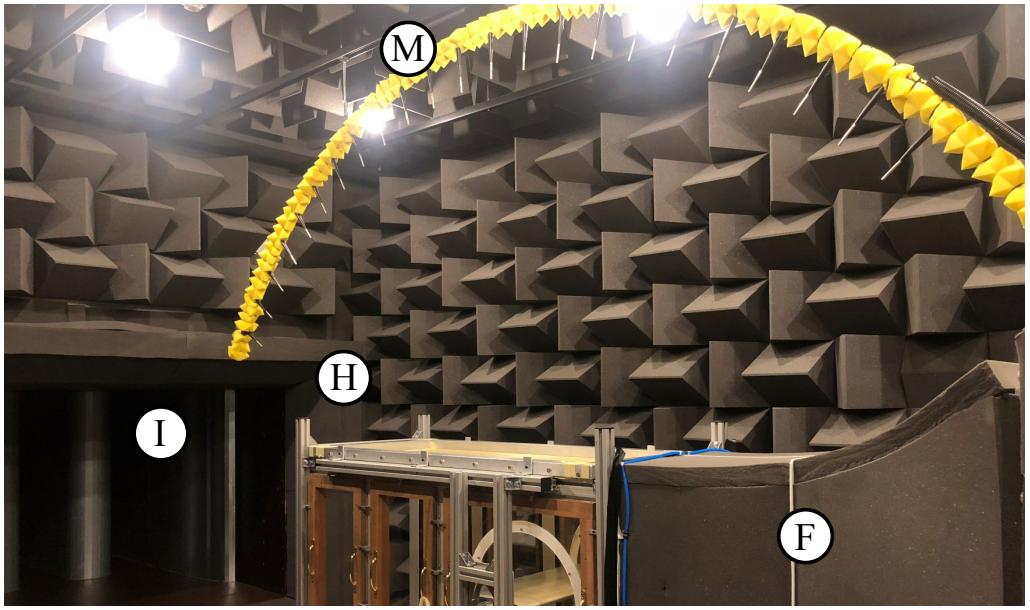

Figure 4: Photograph of the anechoic chamber with a test setup including: (F) Nozzle, (H) Collector, (I) Silencer 3 and (M) far-field microphone arc.

noise studies. Both nozzles also feature angles welded to the outside at the nozzle exit, enabling the mounting of wind tunnel models and other set-ups. All external surfaces of the contraction nozzle and settling chamber are lined with 10 cm thick acoustically absorbing foam sheets. As mentioned previously, it is also possible to fully remove the contraction nozzle and settling chamber to convert the anechoic chamber into a fully anechoic chamber.

2.4.1. Settling Chamber

After the flow has passed the final turning vanes, it expands and enters the settling chamber, see part E in Fig. 1. Two inspection hatches are provided before the settling chamber to provide access to the ductwork and also allow for PIV seeding to be introduced into the flow. Within the settling chamber of 1.8 m × 1.8 m square cross-section the

air flow first passes through a turbulence screen, followed by a honeycomb section and lastly two turbulence screens. The turbulence screens smoothen the flow and reduce the turbulence intensity, whilst the honeycomb section straightens the flow. The first turbulence screen is a plain weave mesh with a mesh opening of 1 mm and 0.5 mm stainless steel wires, whereas the second and third turbulence screen also use a plain weave mesh but with a mesh opening of 1.95 mm and 0.58 mm. The cross-section of the 80 mm thick steel honeycomb section consists of hexagons with a side length of 5.5 mm. Additionally, all four sides of the settling chamber are lined with the same perforated steel sheet as the silencers, with the voids behind the sheets filled in the same manner with compressed acoustic grade mineral wool slab in order to attenuate any noise generated between the last silencer and the settling chamber.

2.4.2. Contraction Nozzles

The careful design of the contraction nozzle is crucial to ensure a high-quality flow at the nozzle exit. Unsteady flow and flow separation must be avoided at both the nozzle inlet and outlet, whilst achieving a low turbulence intensity, low flow angularity and high flow uniformity across the nozzle exit plane is desired [30]. As the high static pressure at the nozzle inlet is converted into dynamic pressure, the turbulent eddies are elongated and the velocity fluctuations are reduced [31]. This is especially important for any nozzle used in an aeroacoustic wind tunnel because an excessively high turbulence intensity can potentially change the nature of the noise generation mechanism, particularly in the case of airfoils. The nozzle design procedure is based on Morel's [32] method of utilizing two polynomials which are connected at a so-called match point for both the width and height profiles of the nozzle. Su [33] extended this method to nozzles with rectangular cross-

sections and investigated the influence of several geometric parameters on the exit flow quality. For a given nozzle length L and a relative match point location of χ, Su defined the centerline distance of the height ($H(X)$) and width ($B(X)$) profiles as a function of the axial distance from the inlet (X), as follows

$$\frac{H(X) - H_2}{H_1 - H_2} = 1 - \frac{(X/L)^{n_1}}{\chi^{n_1 - 1}}, \qquad 0 \leq \frac{X}{L} \leq \chi, \tag{1}$$

$$\frac{H(X) - H_1}{H_2 - H_1} = 1 - \frac{(1 - X/L)^{n_2}}{(1 - \chi)^{n_2 - 1}}, \qquad \chi \leq \frac{X}{L} \leq 1, \tag{2}$$

$$\frac{B(X) - B_2}{B_1 - B_2} = 1 - \frac{(X/L)^{n_1}}{\chi^{n_1 - 1}}, \qquad 0 \leq \frac{X}{L} \leq \chi, \tag{3}$$

$$\frac{B(X) - B_1}{B_2 - B_1} = 1 - \frac{(1 - X/L)^{n_2}}{(1 - \chi)^{n_2 - 1}}, \qquad \chi \leq \frac{X}{L} \leq 1, \tag{4}$$

where H_1 and B_1 are half the inlet height and width, respectively, H_2 and B_2 are half the outlet height and width, respectively, and n_1 and n_2 are the contour powers of the first and second polynomial, respectively. Whilst Su focused on having a common contour power factor ($n_1 = n_2$), it is shown that having a higher contour power factor in the aft part of the nozzle is highly favorable to improve exit flow uniformity [33]. However, having differing contour power factors between the first and second polynomial results in a discontinuous gradient at the match point. In order to avoid this discontinuity in the first derivative, a third order spline is fitted between the two polynomials, reducing the length of the second polynomial curve. The extent of this spline is determined such that the gradient at the beginning of the spline is equal to the gradient at the end of the

spline. This design procedure allows polynomials of different orders to be utilized.

The aeroacoustic facility currently has two nozzles with the exit dimensions of 500 mm × 775 mm and 600 mm × 200 mm. The nozzle inlet has a size of 1.8 m × 1.8 m, resulting in contraction ratios of 8.4 : 1 and 27.0 : 1, respectively. Due to spatial constraints, the contraction nozzles were required to have a common 1 m long first section and an overall length of 2.0 m. In order to achieve a common first section, the first polynomials of the width and height profiles of both nozzles were averaged and the splines connecting the first polynomials to the second polynomials adjusted accordingly. The final width and height profiles of both nozzles can be seen in Figs. 5(a) and 5(b) and the corresponding design parameters are given in Table 6.

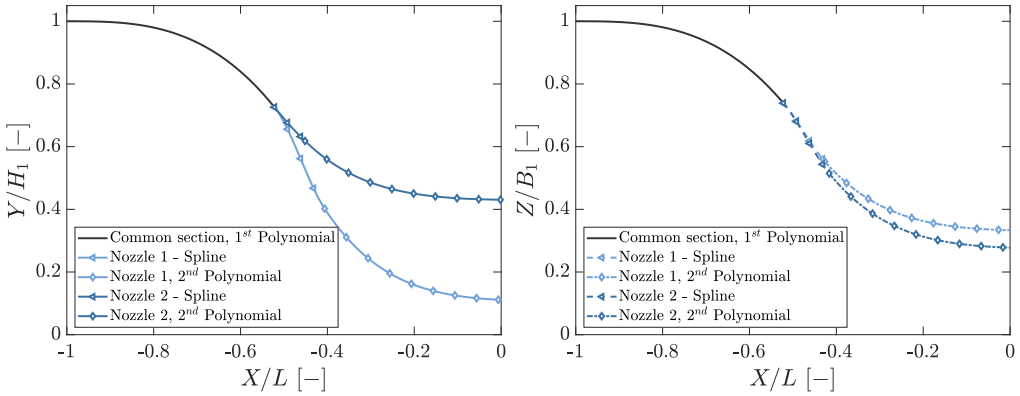

Figure 5: Height (a) and width (b) profiles for both nozzles.

Table 6: Geometric parameters of the two contraction nozzles.

	H_1 [m]	H_2 [m]	B_1 [m]	B_2 [m]	L [m]	n_1	n_2
Nozzle 1	0.9	0.1	0.9	0.3	2	3	5
Nozzle 2	0.9	0.3875	0.9	0.25	2	3	5

In order to assess the aerodynamic performance of the nozzles and also to visualize the flow behavior within the different sections of the contraction nozzles, three-dimensional steady-state $k-\omega$ SST simulations were performed using the open source solver OpenFOAM. The simulations were carried out using a grid of approximately $4.7{\cdot}10^6$ structured cells, with wall functions and an average y^+ of 30 at the nozzle walls for all cases. The simulations were carried out for a jet nozzle exit velocity of $U_\infty = 40\,\mathrm{m/s}$ and $60\,\mathrm{m/s}$ for the $500\,\mathrm{mm} \times 775\,\mathrm{mm}$ nozzle and $600\,\mathrm{mm} \times 200\,\mathrm{mm}$ nozzle, respectively. The inlet turbulence intensity was set to 5 % to investigate the ability of the contraction nozzles to reduce velocity fluctuations sufficiently, achieve a uniform exit flow field and avoid any flow separation. The geometry and coordinate system for the $600\,\mathrm{mm} \times 200\,\mathrm{mm}$ and for the $500\,\mathrm{mm} \times 775\,\mathrm{mm}$ nozzles used in the computations are shown in Fig. 6. The coordinate system origin is placed at the center of the nozzle exit plane, as illustrated in Fig. 6.

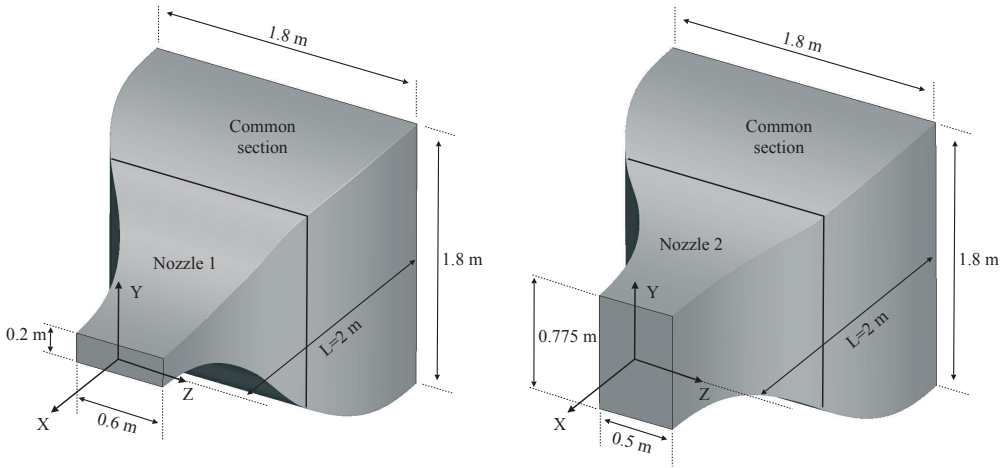

(a) (b)

Figure 6: Isometric view of Nozzle 1 (a) and Nozzle 2 (b) with dimensions and coordinate system.

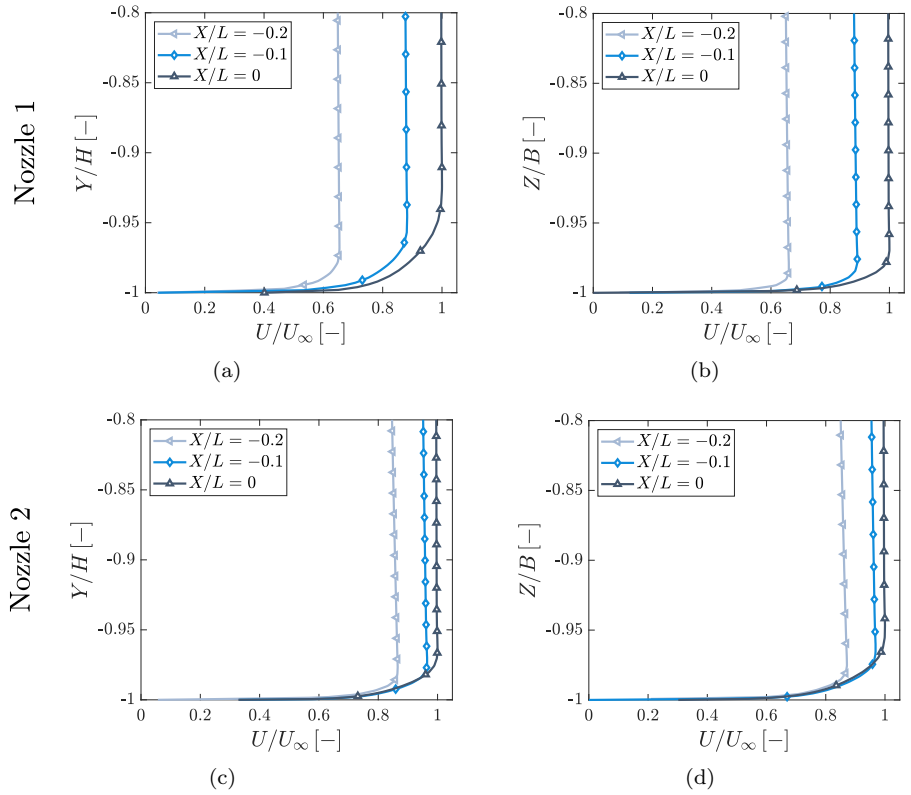

Figure 7: Normalised velocity profiles at three streamwise locations within the nozzle contraction: (a) Nozzle 1, Y-direction, (b) Nozzle 1, Z-direction, (c) Nozzle 2, Y-direction, (d) Nozzle 2, Z-direction. $H(X)$ and $B(X)$ are the nozzle profile functions, given in Eqs. 1-4.

Figure 7 shows the velocity profiles close to the nozzle walls along the Y- and Z-directions for both nozzles at the three streamwise locations of $X/L =$-0.2, -0.1 and 0.0, respectively. The distance from the wall is normalized by the corresponding height and width, namely $H(X)$ and $B(X)$, and hence ranges from -1 to 1. It can be seen that at the exit plane for the smaller nozzle, the velocity is predicted to be uniform over at least 93 % and 97 % of the nozzle extent in the Y- and Z-direction, respectively. The larger nozzle is predicted to produce a uniform flow at the exit plane for 97 % and 96 % of the nozzle extent in the Y- and Z-direction, respectively. Lastly, the velocity contours in the $X - Z$ and $X - Y$ planes within the contraction regions are illustrated in Fig. 8 and it

is clearly shown that there is no flow separation present in the nozzles for the simulated flow conditions.

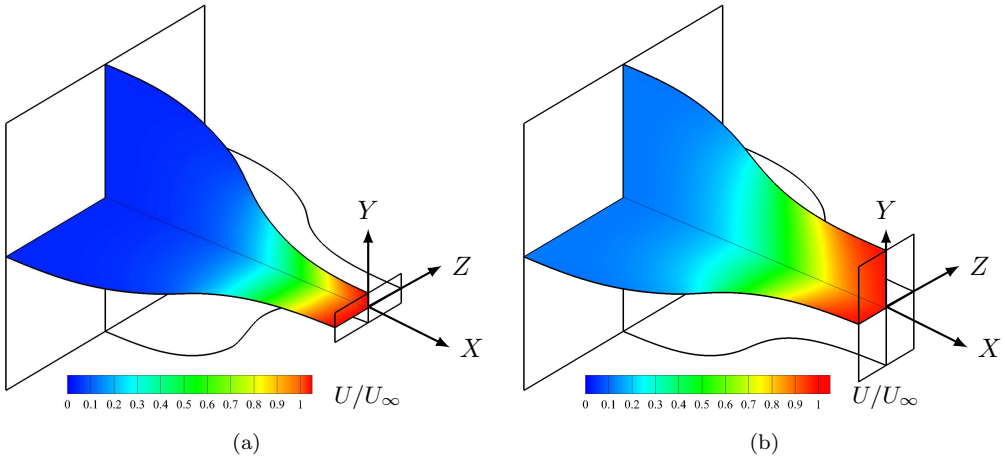

Figure 8: Vertical and horizontal cross-section plane velocity contours: (a) Nozzle 1 at $U_\infty = 60\,\mathrm{m/s}$, (b) Nozzle 2 at $U_\infty = 40\,\mathrm{m/s}$.

3. Aerodynamic and Acoustic Performance Characteristics

3.1. Aerodynamic Characteristics

This section presents the measurements regarding the flow quality of both contraction nozzles. The flow turbulence intensity and uniformity measurements have been conducted using a Dantec 55P16 type hot-wire probe featuring a $5\,\mu$m platinum plated tungsten wire. The hot-wire probe is powered via a Dantec Streamline Pro frame using a CTA91C10 module. The hot-wire probe has been calibrated using a Dantec 54H10 calibrator and the data were captured for 8 seconds at a sampling frequency of 2^{16} Hz using a National Instruments PXIe-4499 card. The hot-wire is moved by means of a

traverse system consisting of two ThorLabs LTS300M stages with 300 mm travel each, whose positioning accuracy is 5 μm. The turbulence intensity (TI) is calculated at each measurement point as

$$TI = U'_{rms}/U_{mean}, \tag{5}$$

where U'_{rms} is the root-mean-square of the velocity fluctuations and U_{mean} is the average velocity. The velocity fluctuations have been high-pass filtered at $f = U_\infty/(2L_{TS})$, where L_{TS} is the largest test section dimension, in order to remove the effect of large-scale facility unsteadiness from the turbulence intensity measurement [34].

3.1.1. Nozzle 1

Figure 9 shows the mean velocity profiles of Nozzle 1 in the horizontal (Z) and vertical (Y) directions at five streamwise distances from the nozzle exit plane for a set velocity of U_∞ = 30 m/s. The horizontal and vertical distances have been normalized by the corresponding nozzle exit parameters (B_2, H_2,) to a range of -1 to 1. Results are presented in terms of the normalized streamwise distance (X/D_h), where D_h = 300 mm is the hydraulic diameter of the nozzle. The velocity results exhibit a top-hat distribution near the nozzle exit, but gradually take a Gaussian shape at further downstream locations, revealing the development of the jet shear layer. The mean velocity does not vary across the horizontal and vertical extent for any of the streamwise distances measured, indicating the presence of a good flow uniformity for the distances considered here. At a distance of $X/D_h = 2.8$, the extent of the free jet with a constant velocity covers 75 % and 40 % of its original extent in the horizontal and vertical directions, respectively. Hence, it can be concluded that the jet potential core has a length in excess of three hydraulic

diameters. It is key for any contraction nozzle to possess a low turbulence intensity at the outlet, in order to facilitate accurate aerodynamic and aeroacoustic measurements and a realistic boundary layer transition behavior. Figure 10 displays the flow turbulence intensity profiles in the horizontal (Z) and vertical (Y) directions for $U_\infty = 30\,\mathrm{m/s}$, which is shown to be as low as 0.09 %. It is visible that the turbulence intensity present in the flow increases for larger nozzle distances as the jet develops. It is worth mentioning that most aeroacoustic tests are carried out with the test rig, *i.e.* airfoil, bluff body, *etc.* placed within the potential core of the jet. As evident in this section, Nozzle 1 produces a good quality air flow, with a high flow uniformity and low turbulence intensity.

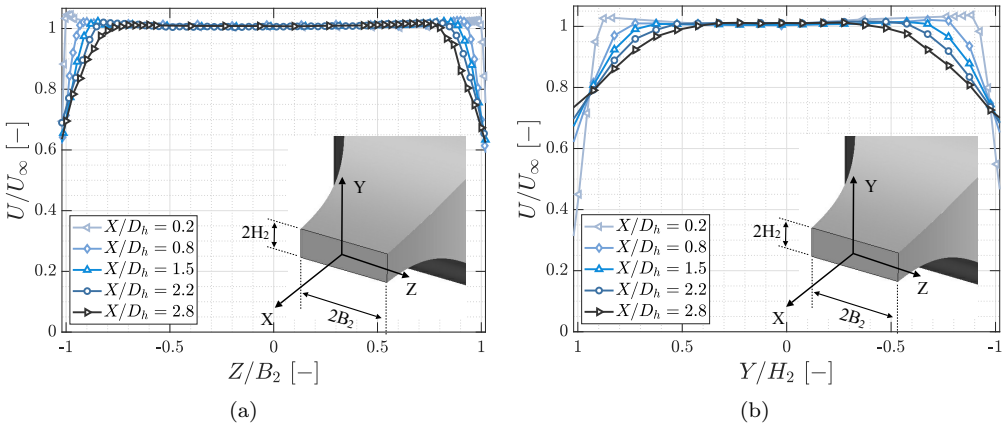

Figure 9: Jet flow velocity profiles in the horizontal (a) and vertical (b) directions at different axial locations for Nozzle 1 at $U_\infty = 30\,\mathrm{m/s}$.

3.1.2. Nozzle 2

Figure 11 provides the mean velocity profiles of Nozzle 2 in the horizontal (Z) and vertical (Y) directions at five distances from the nozzle exit plane for a set velocity of $U_\infty = 30\,\mathrm{m/s}$. The horizontal and vertical distances have been normalized by the corre-

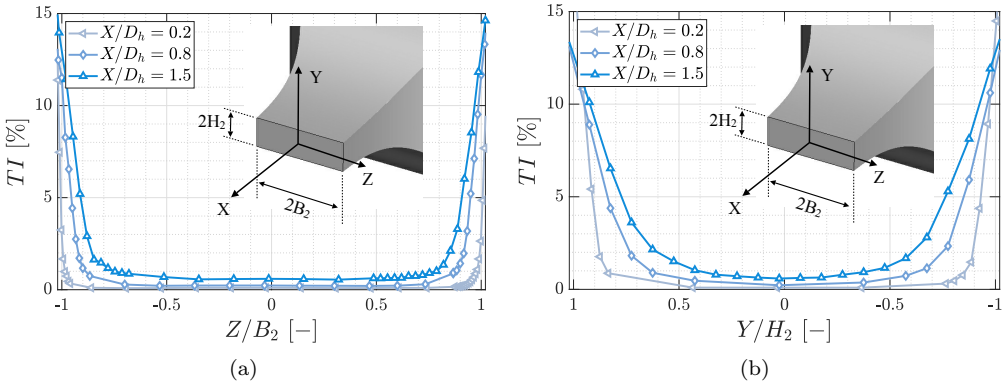

Figure 10: Jet flow turbulence intensity profiles in the horizontal (a) and vertical (b) directions at different axial locations for Nozzle 1 at $U_\infty = 30\,\mathrm{m/s}$.

sponding nozzle exit parameters (B_2, H_2,) to a range of -1 to 1. Results are presented as a function of X/D_h, where $D_h = 608\,\mathrm{mm}$ is the hydraulic diameter of the nozzle. In a comparable way to the smaller nozzle, it can be seen that near the exit plane, the velocity profiles have a top-hat distribution, while with increasing distance, the velocity reduces at the sides of the developing jet. The mean velocity is almost constant across the horizontal and vertical extent for any of the axial distances measured, revealing a good flow uniformity over this region. At a distance of $X/D_h = 1.4$, the velocity remains constant over 77.5 % and 80 % of the horizontal and vertical extent of the nozzle, respectively. Hence, it can be concluded that the potential core has a length well in excess of one and a half hydraulic diameters and noise tests can be carried out by placing objects within this volume. Lastly, Fig. 12 displays the turbulence intensity profiles in the horizontal (Z) and vertical (Y) directions for $U_\infty = 30\,\mathrm{m/s}$, which is found to be as low as 0.12 % and almost constant for 90 % of the horizontal extent for $X/D_h = 0.1$. It is visible that the turbulence intensity increases as the jet develops downstream of the nozzle exit. As seen in this section, Nozzle 2 also produces a good quality air flow, with a high flow

uniformity and low turbulence intensity.

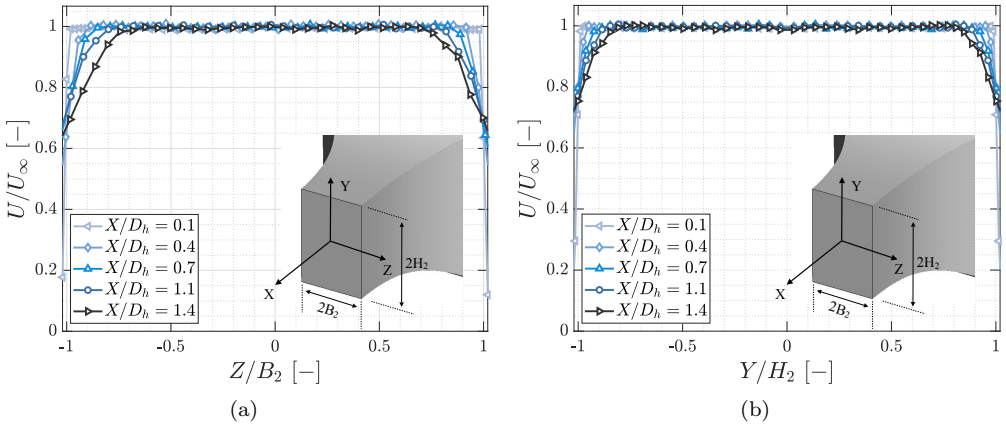

Figure 11: Jet flow velocity profiles in the horizontal (a) and vertical (b) directions at different axial locations for Nozzle 2 at $U_\infty = 30\,\mathrm{m/s}$.

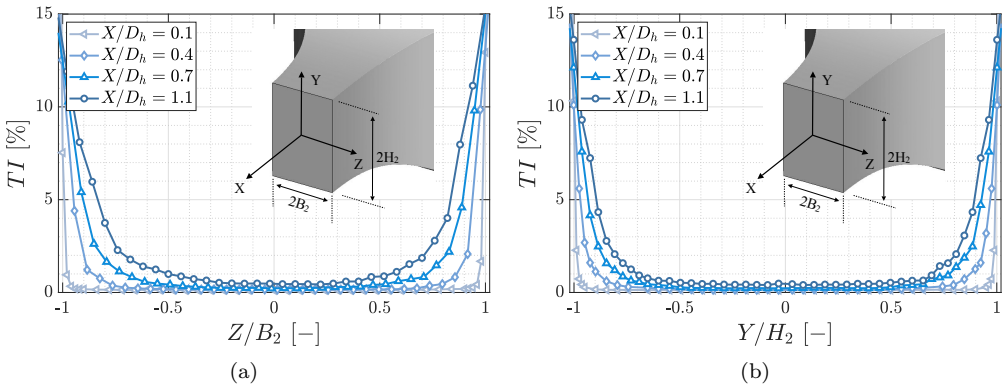

Figure 12: Jet flow turbulent intensity profiles in the horizontal (a) and vertical (b) directions at different axial locations for Nozzle 2 at $U_\infty = 30\,\mathrm{m/s}$.

3.2. Jet flow noise

This section will present the jet flow background noise measurements and associated analysis. It is important for any aeroacoustic facility to have a sufficiently low jet flow

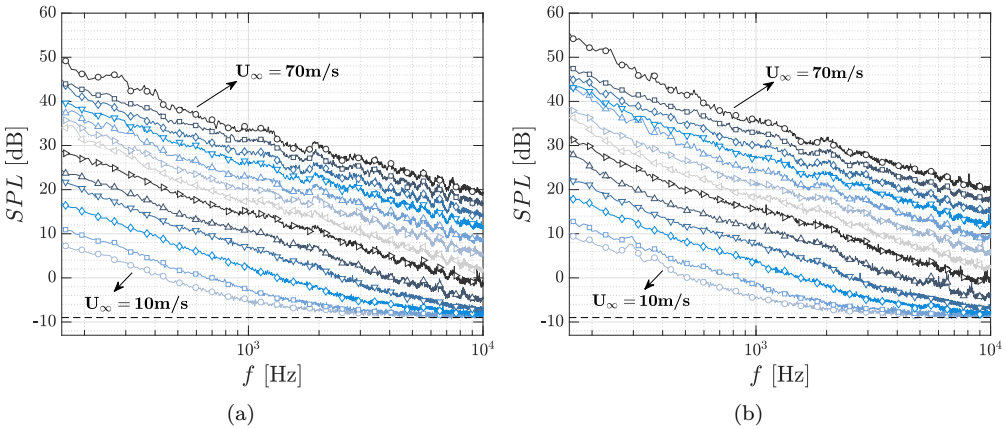

Figure 13: Background noise measurements for the 600 mm × 200 mm nozzle for varying wind speeds from $U_\infty = 10$ m/s to $U_\infty = 70$ m/s at 5 m/s wind speed intervals: (a) $\theta = 90\,^\circ$, (b) $\theta = 45\,^\circ$. The dashed line (**- - -**) shows the noise floor of the anechoic chamber.

background noise, *i.e.* jet flow noise, in order to facilitate good near- and far-field acoustic investigations. For all presented results in this section, microphone signals were acquired for a duration of 16 seconds using three synchronized PXIe-4499 data acquisition cards mounted in a National Instruments PXIe-1062Q chassis. The power spectral density of all presented narrowband noise spectra were calculated using Welch's method and have a frequency bin size of 8 Hz unless indicated otherwise. All spectra are referenced to the reference sound pressure of $20 \cdot 10^{-6}$ Pa. The jet flow background noise analysis focuses on Nozzle 1 which is mainly used for smaller streamlined bodies, but nevertheless background noise levels for Nozzle 2 are also provided in Section 3.3 alongside with noise measurements from some aerodynamic bodies.

Figure 13 depicts the narrowband background noise spectrum for Nozzle 1 for the polar angles of $\theta = 90\,^\circ$ and $45\,^\circ$, respectively. A polar angle of $\theta = 0\,^\circ$ corresponds to a downstream location, aligned with the free stream flow vector, and a polar angle of

$\theta = 90^\circ$ is defined as above the jet flow. As expected, the noise increases for increasing velocities for all frequencies. At velocities of up to $U_\infty = 25\,\mathrm{m/s}$ the background noise reaches the noise floor of the anechoic chamber at approximately -9 dB for high frequencies. In order to ensure that the jet flow noise inside the anechoic chamber is not contaminated by the fan and motor noise, a series of signal coherence studies have been performed. The coherence study was conducted using the signal collected by a microphone placed near the fan/motor and one inside the anechoic chamber above the nozzle. For all velocities investigated ($U_\infty = 10\,\mathrm{m/s}$ - $70\,\mathrm{m/s}$) and the complete frequency range from 160 Hz to 20 kHz, the coherence is below 0.05, indicating almost no acoustic contamination due to external noise sources.

Figure 14 presents the scaling factor of the jet flow background noise, as calculated by

$$N(f) = \log_{10}\left(\frac{S_{pp,U_1}(f)}{S_{pp,U_2}(f)}\right) / \log_{10}\left(\frac{U_1}{U_2}\right), \tag{6}$$

where $S_{pp,U}$ is the power spectral density at the velocity U, U_1 and U_2 are the two velocities for which N is calculated. The curves presented in Fig. 14 show the mean value of N, when calculating Eq. 6 for $U_2 = 70\,\mathrm{m/s}$ and U_1 varying from $30\,\mathrm{m/s}$ to $65\,\mathrm{m/s}$. The results follow a similar trend to the ones presented by Chong *et al.* [19], and it can been seen that for both polar angles considered here the background noise scaling is in excess of 7, clearly showing the contribution of the quadrupole sources of the jet flow to the background noise, which are expected to scale at factor of 8.

Lastly, the A-weighted overall sound pressure level ($OASPL_A$) of the jet flow is

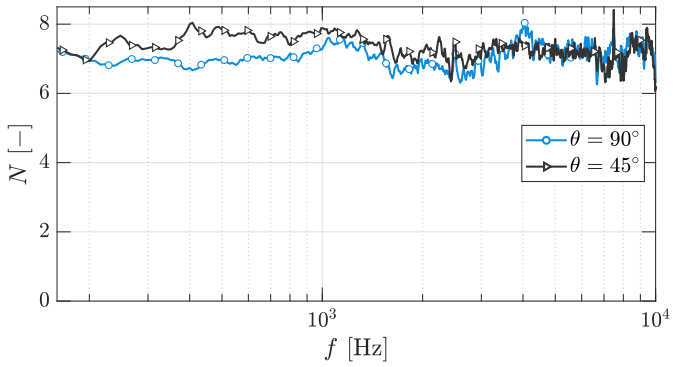

Figure 14: Background noise velocity dependence for two polar angles ($\theta = 45\,°$ and $90\,°$) for Nozzle 1.

compared to the noise data from other aeroacoustic wind tunnels, by means of scaling the $OASPL_A$ according to the following equation,

$$OASPL_{sc,A} = OASPL_A - 10\log_{10}\left(\frac{A}{r^2}\right), \tag{7}$$

where r is the measurement distance from the microphone diaphragm to the center of the nozzle exit plane and A is the nozzle exit cross-sectional area of the respective facility [14, 19, 20]. The A-weighted $OASPL$ is calculated by integrating the narrowband spectra from the cut-off frequency of 160 Hz to 20 kHz, as well as applying the A-weighting corrections [35]. Figure 15 shows the $OASPL_{sc,A}$ comparison, with the data for the other wind tunnels taken from [19, 20]. It is clear that except for $U_\infty = 10\,\mathrm{m/s}$ the Bristol Facility's $OASPL_{sc,A}$ matches or is slightly below the $OASPL_{sc,A}$ of other wind tunnels for both $\theta = 45°$ and $90°$. Starting with $U_\infty = 30\,\mathrm{m/s}$, the $OASPL_{sc,A}$ can be related linearly to the logarithmic velocity. For velocities below $U_\infty = 30\,\mathrm{m/s}$, the narrow spectra show that at high frequencies the jet flow background noise reaches the noise floor of the anechoic chamber, which is a possible explanation for this non-linear behavior.

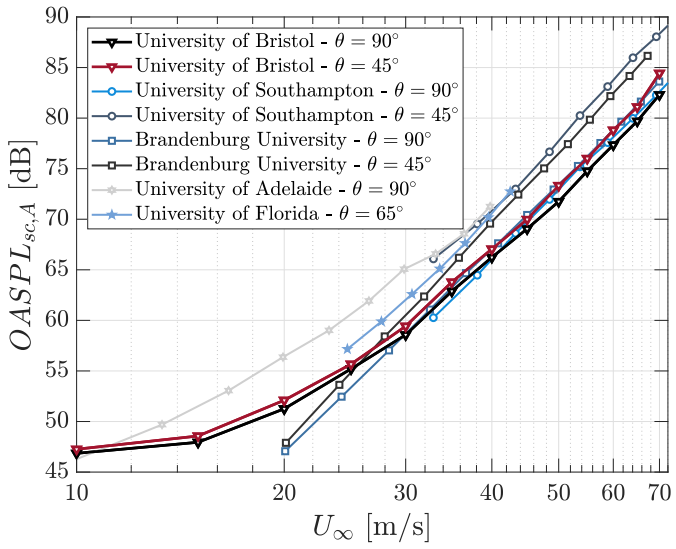

Figure 15: Scaled $OASPL_A$ of various wind tunnels and Nozzle 1. Data taken from [19, 20].

3.3. Benchmark Noise Validation Cases

In the previous sections, we explained the wind tunnel design and provided some information on the aerodynamic performance of the facility. The jet flow background noise was also discussed in Section 3.2. The main purpose of an aeroacoustic facility is to enable far-field noise measurements. In order to demonstrate the capabilities of the University of Bristol's aeroacoustic facility, we have carried out far-field noise measurements for a range of cases, namely a flat plate, a bluff body and a standard NACA 0012 airfoil. In what follows, we will explain each setup and provide the far-field noise data to show the performance of the new facility. Further experimental results for airfoils, high-lift devices and bluff bodies can be found elsewhere [36–40].

3.3.1. Flat Plate

Flat plate studies are of great interest to the aeroacoustic community, allowing a range of fundamental studies to be conducted, such as trailing edge noise, boundary layer noise, hydrodynamic wavenumber-frequency analysis, *etc.* The flat plate test case represents one of the most difficult test cases for evaluating the acoustic performance of the facility, as it is generally very quiet. The far-field noise spectra of a flat plate mounted at the lip-line on Nozzle 1 (600 mm × 200 mm), as well as background noise spectra at a measurement distance of $r = 1.75$ m, are provided in Fig. 16 for the free stream flow velocities of $U_\infty = 20$ m/s, 30 m/s and 40 m/s. Additionally, the scaling factor of the flat plate noise calculated using Eq. 6 for $U_1 = 30$ m/s and $U_2 = 40$ m/s is displayed in Fig. 16 (b). The 50 cm chord flat plate was tripped using a zig-zag tape with a height of 0.5 mm and tip-to-tip distance of 10 mm. The far-field noise results have shown that for all cases considered here, the flat plate trailing edge noise is above the jet background noise. The difference at low frequencies is found to be approximately 10 dB, while at higher frequencies this difference reduces. It is also shown that the scaling factor of the flat plate noise calculated using Eq. 6 is approximately 6 for the entire frequency range, which confirms that turbulent boundary trailing edge noise is the dominant noise source for this test case. These results, therefore, indicate that the background noise levels are sufficiently low enough to facilitate experiments researching flat plate turbulent boundary layer trailing edge noise.

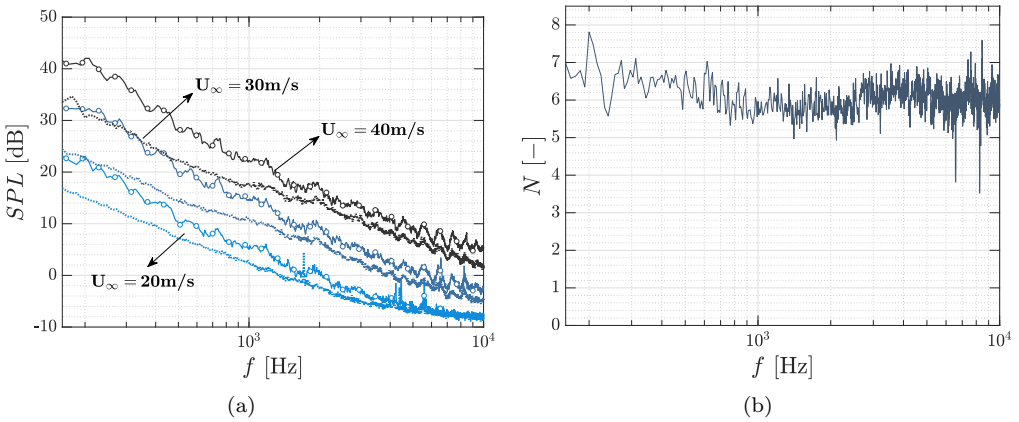

Figure 16: (a) Far-field spectra at θ= 90° of flat plate noise (solid lines with round markers) and background noise (dashed lines) for U_∞ = 20 m/s, 30 m/s and 40 m/s. (b) Flat plate noise scaling factor.

3.3.2. Round Cylinder

The aeroacoustics of bluff bodies is of great academic and industrial interest. Far-field noise measurements using the 600 mm × 200 mm nozzle have been carried out for a cylinder with a diameter of d = 10 mm and a span of 600 mm, resulting in a span to diameter ratio of 60. Figure 17 shows the sound pressure level obtained from the far-field microphones located at θ=45° and 90°, at a distance of r = 1.75 m from the cylinder at the flow velocities of 10 m/s ≤ U_∞ ≤ 60 m/s. The noise radiated from the cylinder was found to be well above the jet flow background noise over the whole frequency range presented in Fig. 17. The vortex shedding peak can be seen at the Strouhal number of $St_d \approx 0.2$ ($St_d = fd/U_\infty$). As demonstrated in other works, the fundamental tonal peak at $St_d \approx 0.2$ is believed to be due to the fluctuating lift force acting on the cylinder [8], while the $St_d \approx$,0.4 peak can be attributed to the fluctuating drag force [41]. The drag force induced tonal noise at $St_d \approx 0.4$ can also clearly be seen in the far-field noise data. Based on the results provided in Fig. 17, it can be concluded that the facility can be used for both fundamental bluff body research, as well as more complex geometries, such

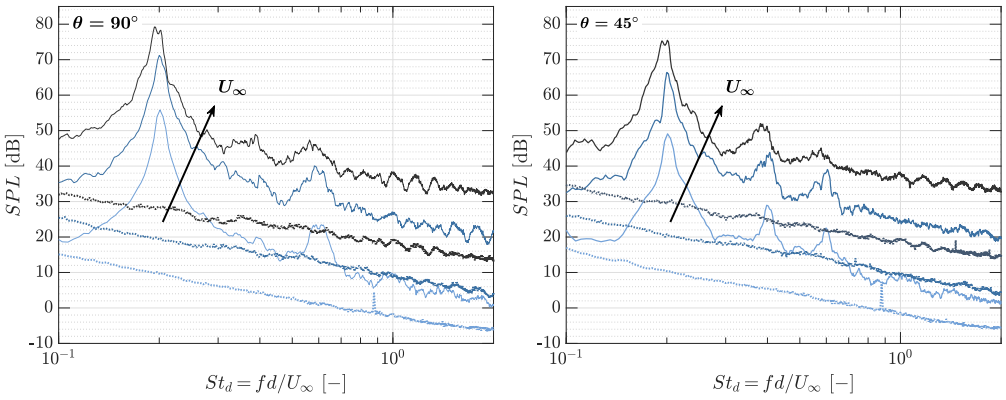

Figure 17: Far-field noise spectra for cylinder with a diameter of $d = 10\,\text{mm}$ (solid lines) and background noise (dotted lines) for $U_\infty = 20\,\text{m/s}$, $40\,\text{m/s}$ and $60\,\text{m/s}$ at two polar angles: (a) $\theta = 90°$, (b) $\theta = 45°$.

as landing gear systems, car side mirror, *etc.*

3.3.3. Tripped NACA 0012 Airfoil

The symmetric NACA 0012 airfoil is one of the most often studied airfoils and has therefore been selected as one of the benchmark test cases for this new facility. The one-third-octave band far-field noise spectra of a NACA 0012 airfoil at an angle of attack of $\alpha = 1.5\,°$ is compared to the BPM turbulent boundary layer trailing edge noise model [42]. The jet flow background noise is also provided for comparison for wind speeds of $U_\infty = 30\,\text{m/s}$ and $40\,\text{m/s}$, at $\theta = 90°$ and at a measurement distance of $r/c = 11.7$, see Fig. 18. Additionally, Fig. 18 displays experimental data from Brooks *et al.* [42] for a tripped NACA 0012 airfoil with a chord of $15.24\,\text{cm}$, at an angle of attack of $\alpha = 0\,°$ and wind speeds of $U_\infty = 32\,\text{m/s}$ and $40\,\text{m/s}$. The data has been corrected to match the present experimental conditions regarding the airfoil span and measurement distance. The airfoil with a chord length of $15\,\text{cm}$ and a span of $60\,\text{cm}$ was mounted between two

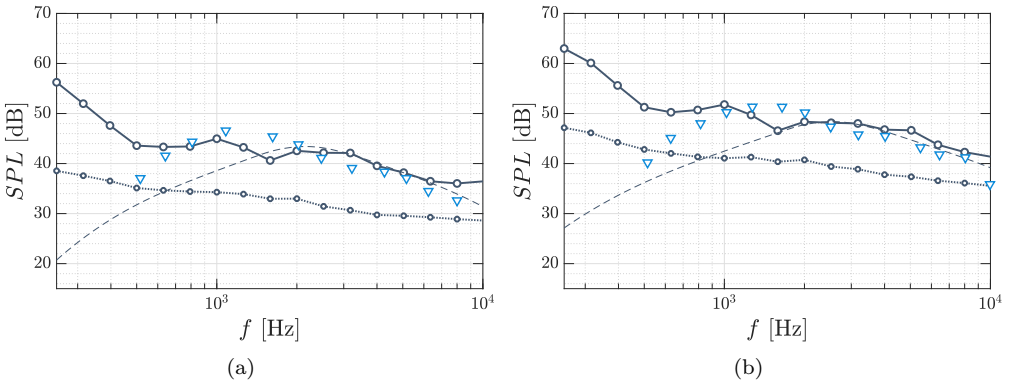

Figure 18: Far-field spectra in 1/3 octave bands at $\theta = 90°$ for a NACA 0012 airfoil (solid line with round markers), BPM model (dashed line), Brooks' *et al.* data [42] (triangular markers) and background noise (dashed line with round markers): (a) $U_\infty = 30$ m/s and (b) $U_\infty = 40$ m/s.

side-plates in Nozzle 1 (600 mm × 200 mm), at a distance of 30 cm (*i.e.* two chord-lengths) from the nozzle exit in the streamwise direction. The airfoil was tripped by means of a 6 mm wide and 0.5 mm thick zig-zag turbulator trip tape with a turbulator angle of 70° from Glasfaser-Flugzeug-Service GmbH at 10% of the chord [43]. The required boundary layer thickness for the BPM model was calculated using XFoil [44]. For all velocities, the noise emitted from the airfoil was found to exceed the background noise by more than 10 dB and matches well with the experimental data by Brooks' *et al.*, as illustrated in in Fig. 18. It can also be observed that the airfoil far-field noise spectra match the BPM predictions well at mid and high frequencies. The mismatch at low frequencies has also been reported by others using different facilities and is believed to be due to low frequency noise amplification of the jet noise when the airfoil is placed inside the flow [19–21, 45]. These results for a small chord NACA 0012 airfoil indicate that the facility can be used to investigate the trailing edge noise emitted from airfoils.

4. Conclusions

An overview of the design and the aerodynamic and acoustic performance of the University of Bristol Aeroacoustic Facility has been presented in this paper. The various acoustic and aerodynamic features of facility have been described, such as the silencers, fan and settling chamber and nozzles. The anechoic chamber has been certified to be anechoic down to 160 Hz. This characteristic together with low background noise and the two contraction nozzles with a high flow quality, make this facility versatile for a variety of aeroacoustic measurements, such as airfoil noise, noise from bluff bodies and instability noise studies. The far-field noise results from a flat plate, a round cylinder and a NACA 0012 airfoil have been presented and discussed to demonstrate the capabilities of the facility. The facility is expected to be used for a wide range of fundamental as well as industrial studies.

Declaration of interest

None.

Acknowledgement

The authors would like to gratefully acknowledge the significant investment in this aeroacoustic wind tunnel facility from the University of Bristol through the Capital Investment Programme Board (CIPB).

References

[1] Y. Mayer, H. Kamliya Jawahar, M. Szoke, M. Azarpeyvand, Design of an Aeroacoustic Wind Tunnel Facility at the University of Bristol, in: 2018 AIAA/CEAS Aeroacoustics Conference, AIAA 2018-3138, Atlanta, Georgia, United States, 2018. doi:10.2514/6.2018-3138.

[2] E. Koppen, K. Fowler, International Legislation for Wind Turbine Noise, in: Euronoise 2015, Maastricht, Netherlands, 2015, pp. 321–326.

[3] M. J. T. Smith, Aircraft Noise, Cambridge Aerospace Series, Cambridge University Press, Cambridge, United Kingdom, 1989. doi:10.1017/CBO9780511584527.

[4] F. Avallone, W. C. P. van der Velden, D. Ragni, Benefits of curved serrations on broadband trailing-edge noise reduction, Journal of Sound and Vibration 400 (2017) 167–177. doi:10.1016/j.jsv.2017.04.007.

[5] M. Azarpeyvand, M. Gruber, P. F. Joseph, U. Kingdom, An analytical investigation of trailing edge noise reduction using novel serrations, in: 19th AIAA/CEAS Aeroacoustics Conference, Berlin, Germany, 2013. doi:10.2514/6.2013-2009.

[6] D. J. Moreau, C. J. Doolan, Noise-Reduction Mechanism of a Flat-Plate Serrated Trailing Edge, AIAA Journal 51 (2013). doi:10.2514/1.J052436.

[7] X. Liu, H. K. Jawahar, M. Azarpeyvand, R. Theunissen, Aerodynamic Performance and Wake Development of Airfoils with Serrated Trailing-Edges, AIAA Journal 55 (2017) 3669–3680. doi:10.2514/1.J055817.

[8] T. F. Geyer, E. Sarradj, Circular cylinders with soft porous cover for flow noise reduction, Experiments in Fluids 57 (2016). doi:10.1007/s00348-016-2119-7.

[9] S. A. S. Ali, M. Azarpeyvand, C. R. I. Da Silva, Trailing-edge flow and noise control using porous treatments, Journal of Fluid Mechanics 850 (2018) 83–119. doi:10.1017/jfm.2018.430.

[10] T. Wolff, B. Ernst, J. R. Seume, Aerodynamic behavior of an airfoil with morphing trailing edge for wind turbine applications, in: The Science of Making Torque from Wind 2014 (Torque 2014), Copenhagen, Denmark, 2014. doi:10.1088/1742-6596/524/1/012018.

[11] Q. Ai, M. Azarpeyvand, X. Lachenal, P. M. Weaver, Aerodynamic and aeroacoustic performance of airfoils with morphing structures, Wind Energy 19 (2016) 1325–1339. doi:10.1002/we.

[12] M. Szoke, D. Fiscaletti, M. Azerpeyvand, Effect of inclined transverse jets on trailing- edge noise

generation, Physics of Fluids 30 (2018). doi:10.1063/1.5044380.

[13] B. Arnold, T. Lutz, E. Krämer, C. Rautmann, Wind-Turbine Trailing-Edge Noise Reduction by Means of Boundary-Layer Suction, AIAA Journal 56 (2018) 1843–1854. doi:10.2514/1.J056633.

[14] E. Duell, J. Walter, S. Arnette, J. Yen, Recent Advances in Large Scale-Aeroacoustic Wind Tunnels, in: 8th AIAA/CEAS Aeroacoustics Conference & Exhibit, AIAA 2002-2503, Breckenridge, Colorado, United States, 2002. doi:10.2514/6.2002-2503.

[15] T. Dassen, R. Parchen, J. Bruggeman, Wind tunnel measurements of the aerodynamic noise of blade sections, in: Proceedings of the European Wind Energy Conference and Exhibition, Thessaloniki, Greece, 1993, pp. 791–798.

[16] H. H. Hubbard, J. C. Manning, Aeroacoustic Research Facilities at NASA Langley Research Center: Description and Operational Characteristics, Technical Report, NASA Langley Research Center, Hampton, Virginia, United States, 1983.

[17] F. Mery, Low speed anechoic closed test section at ONERA S1MA Wind tunnel, in: 22nd AIAA/CEAS Aeroacoustics Conference, AIAA 2016-2895, Lyon, France, 2016. doi:10.2514/6.2016-2895.

[18] M. Pott-Pollenske, J. Delfs, Enhanced Capabilities of the Aeroacoustic Wind Tunnel Braunschweig, in: 14th AIAA/CEAS Aeroacoustics Conference (29th AIAA Aeroacoustics Conference), AIAA 2008-2910, Vancouver, British Columbia, Canada, 2008. doi:10.2514/6.2008-2910.

[19] T. Chong, P. Joseph, P. Davies, Design and performance of an open jet wind tunnel for aeroacoustic measurement, Journal of Applied Acoustics 70 (2009) 605–614. doi:10.1016/j.apacoust.2008.06.011.

[20] E. Sarradj, C. Fritzsche, T. Geyer, J. Giesler, Acoustic and aerodynamic design and characterization of a small-scale aeroacoustic wind tunnel, Journal of Applied Acoustics 70 (2009) 1073–1080. doi:10.1016/j.apacoust.2009.02.009.

[21] A. Vathylakis, J. H. Kim, T. P. Chong, Design of a low-noise aeroacoustic wind tunnel facility at Brunel University, in: 20th AIAA/CEAS Aeroacoustics Conference, AIAA 2014-3288, Atlanta, Georgia, United States, 2014. doi:10.2514/6.2014-3288.

[22] D. Leclercq, C. Doolan, J. Reichl, Development and Validation of a Small-Scale Anechoic Wind Tunnel, in: ICSV14: Proceedings of the 14th International Congress on Sound and Vibration, Cairns, Australia, 2007.

[23] K. Pascioni, R. Reger, A. Edstrand, L. Cattafesta, Characterization of an Aeroacoustic Wind Tunnel Facility, in: 43rd International Congress on Noise Control Engineering November, Melbourne, Australia, 2014.

[24] J. Winkler, T. Carolus, Concept, design and characterization of a small aeroacoustic wind tunnel facility with application to airfoil measurements, Noise Control Engineering Journal 57 (2009) 370–383. doi:10.3397/1.3151911.

[25] C. Doolan, D. Moreau, M. Awasthi, C. Jiang, The UNSW Anechoic Wind Tunnel, in: Acoustics 2018, Adelaide, Australia, 2018.

[26] T. Mueller, D. Scharpf, S. Batill, C. Sullivan, S. Subramanian, The Design of a Subsonic Low-Noise, Low-Turbulence Wind Tunnel for Acoustic Measurements, in: AIAA 17th Aerospace Ground Testing Conference, AIAA 92-3883, Nashville, Tennessee, USA, 1992. doi:10.2514/6.1992-3883.

[27] S. S. Moreau, M. Roger, Effect of Airfoil Aerodynamic Loading on Trailing Edge Noise Sources, AIAA Journal 43 (2005) 41–52. doi:10.2514/1.5578.

[28] W. J. Devenport, R. A. Burdisso, A. Borgoltz, P. A. Ravetta, M. F. Barone, K. A. Brown, M. A. Morton, The Kevlar-walled anechoic wind tunnel, Journal of Sound and Vibration 332 (2013) 3971–3991. doi:10.1016/j.jsv.2013.02.043.

[29] M. Murayama, Y. Yokokawa, H. Ura, K. Nakakita, K. Yamamoto, Y. Ito, T. Takaishi, R. Sakai, K. Shimoda, T. Kato, T. Homma, Experimental Study of Slat Noise from 30P30N Three-Element High-Lift Airfoil in JAXA Kevlar-Wall Low-Speed Wind Tunnel, in: 2018 AIAA/CEAS Aeroacoustics Conference, AIAA 2018-3460, Atlanta, Georgia, United States, 2018, pp. 1–30. doi:10.2514/6.2018-3460.

[30] M. N. Mikhail, Optimum Design of Wind Tunnel Contractions, AIAA Journal 17 (1979) pp. 471–477. doi:10.2514/3.61157.

[31] S. B. Pope, Turbulent Flows, Cambridge University Press, Cambridge, Massachusetts, United States, 2000. doi:10.1017/CBO9780511840531.

[32] T. Morel, Comprehensive Design of Axisymmetric Wind Tunnel Contractions, Journal of Fluids Engineering 97 (1975) 225–233. doi:10.1115/1.3447255.

[33] Y. Su, Flow analysis and design of three-dimensional wind tunnel contractions, AIAA Journal 29 (1991) 1912–1920. doi:10.2514/3.10818.

[34] L. Cattafesta, C. Bahr, J. Mathew, Fundamentals of Wind-Tunnel Design, in: Encyclopedia of

Aerospace Engineering, 2010. doi:10.1002/9780470686652.eae532.

[35] T. D. Rossing (Ed.), Handbook of Acoustics, 2nd ed., Springer Science & Business Media, 2014. doi:10.1007/978-1-4939-0755-7.

[36] Y. D. Mayer, B. Zang, M. Azarpeyvand, Aeroacoustic Characteristics of a NACA 0012 Airfoil for Attached and Stalled Flow Conditions, in: 25th AIAA/CEAS Aeroacoustics Conference, Delft, The Netherlands, 2019.

[37] B. Zang, Y. D. Mayer, M. Azarpeyvand, An Experimental Investigation on the Mechanism of Tollmien-Schlichting Waves for a NACA 0012 Aerofoil, in: 25th AIAA/CEAS Aeroacoustics Conference, Delft, The Netherlands, 2019.

[38] H. K. Jawahar, S. S. Ali, M. Azarpeyvand, C. Silva, Aeroacoustic Performance of High-lift Airfoil with Slat Cove Fillers, in: 25th AIAA/CEAS Aeroacoustics Conference, Delft, The Netherlands, 2019.

[39] A. Celik, B. Zang, Y. D. Mayer, X. Liu, M. Azarpeyvand, Hydrodynamic Analysis of Trailing Edge Serrations with Blunt and Rounded Edges, in: 8th Internation Conference on Wind Turbine Noise, Lisbon, Portugal, 2019.

[40] Y. D. Mayer, B. Zang, M. Azarpeyvand, Design of a Kevlar-Walled Test Section with Dynamic Turntable and Aeroacoustic Investigation of an Oscillating Airfoil, in: 25th AIAA/CEAS Aeroacoustics Conference, Delft, The Netherlands, 2019.

[41] W. R. Wolf, Airfoil Aeroacoustics: LES and Acoustic Analogy Predictions, Ph.D. thesis, Stanford University, 2011.

[42] T. F. Brooks, D. S. Pope, M. A. Marcolini, Airfoil Self-Noise and Prediction, Technical Report, NASA Langley Research Center, Hampton, Virginia, United States, 1989. doi:10.1111/j.1469-7580.2012.01504.x.

[43] H. Streifeneder, Glasfaser-Flugzeug-Service GmbH, 2018. URL: http://www.streifly.de/shopbaender-d.htm.

[44] M. Drela, XFOIL: An Analysis and Design System for Low Reynolds Number Airfoils, in: Low Reynolds Number Aerodynamics: Proceedings of the Conference Notre Dame, Notre Dame, Indiana, United States, 1989.

[45] R. C. N. Leung, P. Chaitanya, P. F. Joseph, Effect of aerofoil thickness on trailing edge noise, in: 22nd AIAA/CEAS Aeroacoustics Conference, AIAA 2016-2814, Lyon, France, 2016. doi:10.2514/

6.2016-2814.